Ab initio prediction of an order-disorder transition in math xmlns="http://www.w3.org/1998/Math/MathML">mrow>msub>mi>Mg/mi>mn>2/mn>/msub>mi>Ge/mi>msub>mi mathvariant="normal">O/mi>mn>4/mn>/msub>/mrow>/math>: Implication for the nature of super-Earth's mantles

Koichiro Umemoto and Renata M. Wentzcovitch

Phys. Rev. Materials **5**, 093604 — Published 8 September 2021

DOI: 10.1103/PhysRevMaterials.5.093604

Ab initio prediction of an order-disorder transition in Mg_2GeO_4: implication for the nature of super-Earth's mantles

Koichiro Umemoto[1,2], and Renata M. Wentzcovitch[3,4]

[1] *Earth-Life Science Institute, Tokyo Institute of Technology, Tokyo, Japan*

[2] *Theoretical Quantum Physics Laboratory, Cluster for Pioneering Research, RIKEN, Wako-shi, Saitama 351-0198, Japan*

[3] *Department of Applied Physics and Applied Mathematics, Columbia University, New York, NY, USA.*

[4] *Department of Earth and Environmental Sciences, Lamont Doherty Earth Observatory, Columbia University, New York, NY, USA.*

(Dated: July 29, 2021)

Abstract

Here we present an *ab initio* prediction of an order-disorder transition (ODT) from $I\bar{4}2d$-type to a Th_3P_4-type phase in the cation sublattices of Mg_2GeO_4, a post-post-perovskite (post-PPv) phase. This uncommon type of prediction is achieved by carrying out a high-throughput sampling of atomic configurations in a 56-atom supercell followed by a Boltzmann ensemble statistics calculation. Mg_2GeO_4 is a low-pressure analog of $I\bar{4}2d$-type Mg_2SiO_4, a predicted major planet-forming phase of super-Earths' mantles. Therefore, a similar ODT is anticipated in $I\bar{4}2d$-type Mg_2SiO_4 as well, which should impact the internal structure and dynamics of these planets. The prediction of this Th_3P_4-type phase in Mg_2GeO_4 enhances further the relationship between the crystal structures of Earth/planet-forming silicates and oxides at extreme pressures and those of rare-earth sesquisulfides at low pressures.

I. INTRODUCTION

Ab initio quasiharmonic (QHA) calculations of polymorphic phase transitions at extreme pressure and temperature conditions have proven to be highly predictive for nearly two decades [1]. Combined with materials discovery methods (e.g., Refs. [2–7]), these simulation tools offer a powerful approach to investigating phase transition phenomena at challenging experimental conditions typical of planetary interiors. Mineral physics and geophysics have benefitted immensely from these developments in materials simulations in the past two decades. For example, in 2004, *ab initio* predictions played a crucial role in discovering and elucidating the major post-perovskite (PPv) transition in $MgSiO_3$ bridgmanite at deep Earth interior conditions, e.g., 2,500K at 125 GPa [8–10]. More recently, *ab initio* QHA calculations have explored pressure and temperature conditions expected in interior of super-Earths, terrestrial-type exoplanets more massive than Earth. The interest in these planets stems from their similarities and differences with Earth and their potential habitability. Besides, *ab initio* methods are highly predictive when addressing planet-forming silicates and oxides, motivating experiments. These phases are oxides involving Mg, Si, ferrous and ferric Fe, Al, and Ca, primarily. In deep interiors of large super-Earths with up to ∼13 Earth mass ($M_\oplus$), the range of pressures and temperatures can reach tens of tera-Pascals (TPa) (hundreds of Mbar) and 10^4–10^5 K [11, 12]. Despite remarkable developments in experimental techniques [13–17], these pressure-temperature conditions are still very challenging to experiments making *ab initio* predictions of phase transition phenomena in planet-forming phases critical to advancing planetary modeling. This progress has been registered in a series of *ab initio* discoveries concerning the nature of super-Earth's mantle-forming phases in the important MgO-SiO_2 system [6, 18–21]. They have culminated in partial experimental confirmations in a low-pressure analog system, NaF-MgF_2 [22], and detailed modeling of these planets' internal structure and dynamics [11, 12]. In particular, a sequence of "post-post-perovksite" (post-PPv) transitions in the MgO-SiO_2 system [6, 18–21] was predicted to occur up to ∼3 TPa and 10,000 K, starting from $MgSiO_3$ PPv and ending in its dissociation into the elementary oxides MgO and SiO_2. This dissociation process was predicted to occur in three stages: 1) a dissociation reaction, $MgSiO_3$ PPv → $I\bar{4}2d$-type Mg_2SiO_4 + $P2_1/c$-type $MgSi_2O_5$; 2) further dissociation of $P2_1/c$-type $MgSi_2O_5$ → $I\bar{4}2d$-type Mg_2SiO_4 + Fe_2P-type SiO_2; 3) final dissociation of $I\bar{4}2d$-type Mg_2SiO_4 →

CsCl-type MgO + Fe_2P-type SiO_2. If $MgSiO_3$ coexists with MgO or SiO_2, other intermediate recombination reactions producing Mg_2SiO_4 or $MgSi_2O_5$ can intervene in the three-stage dissociation process. These post-PPv transitions were shown to have profound effects on super-Earths' mantle dynamics [11, 12]. However, the exceedingly high predicted transition pressures ($>\sim$ 500 GPa) make their experimental confirmation quite challenging.

Two potential low-pressure analog systems, i.e., MgO-GeO_2 and NaF-MgF_2, were proposed as viable experimental alternates [23, 24]. Both displayed some of these novel high-pressure phases found in the MgO-SiO_2 system. $NaMgF_3$ PPv was predicted to exhibit the novel $P2_1/c$-type structure of $MgSi_2O_5$ under pressure before its full dissociation into NaF and MgF_2. The predicted phases and transformations were experimentally confirmed [22]. In contrast, $MgGeO_3$ PPv under pressure was expected to produce the novel $I\bar{4}2d$-type Mg_2SiO_4 structure. The predicted reactions in the MgO-GeO_2 system have not been experimentally confirmed yet since they happen at higher pressures. At low temperature, experimental observation of these dissociation and recombination transitions might be intervened by a polymorphic transition from PPv to Gd_2S_3-type or U_2S_3-type post-PPv phase [21–24]. Also, both systems were expected to display the respective analog recombination reactions. This state of affairs brings us to our present study.

Using *ab initio* techniques, we predict another type of phase transition in the MgO-GeO_2 system, a temperature-induced change from the tetragonal $I\bar{4}2d$-type to the cubic Th_3P_4-type ($I\bar{4}3d$-type) structure in Mg_2GeO_4. This is not a regular polymorphic phase transition but an order-disorder transition (ODT) in the cation sublattices.

The result predicted here is unexpected since disorder occurs between two sublattices containing cations with nominally different valences. Specifically, Mg and Ge are known to form stoichiometric end-member phases (MgO and GeO_2), preserving their nominal valence at comparable pressures. This type of prediction is also uncommon since it requires reliable methods to compute free energy in disordered solid-solutions, which is computationally much more costly than regular polymorphic transitions. The predicted pressure and temperature transition conditions for this ODT are more easily achievable in laboratory experiments than the analog one in Mg_2SiO_4.

II. CRYSTAL STRUCTURES OF Mg_2GeO_4

The crystal structure of $I\bar{4}2d$-type Mg_2GeO_4 is shown in Fig. 1. As far as we know, this structure has not been identified experimentally so far. This phase is body-centered-tetragonal and its space group is $I\bar{4}2d$. In the $I\bar{4}2d$-type phase, both Mg and Ge cations are regularly ordered; Mg and Ge ions are at $8d$ and $4b$ Wyckoff positions, respectively. Local atomic environments around the Mg and Ge sites are very similar, both being surrounded by eight O ions (Fig. 1(b)). The eight-fold coordinated polyhedra are somewhat intermediate between NaCl-type octahedra and CsCl-type cubes. The $I\bar{4}2d$-type structure is related to that of Zn_2SiO_4-II [25]. While the cation arrangements in Zn_2SiO_4-II are identical to those of $I\bar{4}2d$-type Mg_2GeO_4, the anion arrangement differs. In Zn_2SiO_4-II, cations are surrounded by four O ions. Average Mg-O and Ge-O bondlengths are 1.788 Å and 1.780 Å at 400 GPa, respectively. This similarity suggests that only a relatively small elastic strain energy would be generated by disordering Mg and Ge ions and configuration entropic effects could stabilize a disordered phase in Mg_2GeO_4 at high temperatures. Such disordered phase is cubic and its space group is $I\bar{4}3d$, a supergroup of $I\bar{4}2d$. The structure of this disordered phase is identical to that of Th_3P_4. In this structure, cations are in the $12a$ (3/8, 0, 1/4) Wyckoff sites.

III. COMPUTATIONAL METHOD

A. Statistical treatment

The ODT critical temperature, T_c, was calculated using the same approach previously used to compute the ice-VII to -VIII ODT boundary [26]. To represent the disordered Th_3P_4-type phase in a supercell of the conventional $I\bar{4}2d$-type unit cell, we generated an ensemble of N_{conf} irreducible configurations using the scheme described in the next subsection. We then computed the static partition function for the configuration ensemble:

$$Z_{static}(V,T) = \sum_{i=1}^{N_{conf}} w_i \exp\left(-\frac{E_i(V)}{k_B T}\right), \tag{1}$$

where $E_i(V)$ and w_i are the total energy and multiplicity of the ith irreducible configuration, and k_B is the Boltzmann's constant. The total energies $E_i(V)$ in this case were obtained by

fully relaxing the cell shape and atomic positions. The static partition function is then extended to include zero-point motion (ZPM) and phonon thermal excitation energies within the QHA [26, 35]. From $Z(V,T)$, all thermodynamic potentials and functions can be calculated: Helmholtz free energy $F(V,T) = -k_B T \ln Z$, pressure $P(V,T) = -(\partial F/\partial V)_T$, Gibbs free energy $G(V,T) = F+PV$ (converted to $G(P(V,T),T)$), entropy $S(V,T) = -(\partial F/\partial T)_V$, constant-volume heat capacity $C_V(V,T) = T(\partial S/\partial T)_V$, constant-pressure heat capacity $C_P(P,T) = T(\partial S/\partial T)_P$, and so forth. Several thermodynamic quantities are listed in Table S1 for both Th_3P_4-type and $I\bar{4}2d$-type phases. Finally the ODT is obtained by locating a peak in $C_P(T)$.

In addition to a peak in $C_P(T)$, the ODT can be captured by the probability of occurrence of the ith irreducible configuration (P_i) given by

$$P_i(V,T) = \frac{w_i \exp\left(-\frac{E_i(V)}{k_B T}\right)}{Z(V,T)}. \tag{2}$$

For the ordered $I\bar{4}2d$-type phase, $P_{I\bar{4}2d} \sim 1$ and $P_i \sim 0$. Above T_c, all P_i's become similar, indicating the disordered Th_3P_4-type phase. The probability of occurrence of a Mg atom at the Mg and Ge sites, i.e., $[\mathrm{Mg}]_{\mathrm{Mg}}$ and $[\mathrm{Mg}]_{\mathrm{Ge}}$, here defined as $q^{\mathrm{Mg}}_{\mathrm{Mg}}$ and $q^{\mathrm{Mg}}_{\mathrm{Ge}}$, is calculated by taking the average of $\sigma_{j,k}$, where $\sigma_{j,k} = 1$ when Mg exists at the jth Mg site in configuration k, one of the w_i configurations symmetrically equivalent to the ith irreducible configuration; $\sigma_{j,k} = 0$ if Mg exists at the jth Ge site:

$$q_{\mathrm{Mg(Ge)\,site}} = \sum_{i=1}^{N_{conf}} P_i \frac{1}{N_{\mathrm{Mg(Ge)}}} \sum_{j=1}^{N_{\mathrm{Mg(Ge)}}} \frac{1}{w_i} \sum_{k=1}^{w_i} \sigma_{j,k}, \tag{3}$$

where $N_{\mathrm{Mg(Ge)}}$ is the number of the Mg (Ge) sites in the $I\bar{4}2d$-type structure.

B. Configuration ensembles

To calculate the partition function in Eq. 1 and then T_c, we need to sample configurations in an efficient way. We start by checking the convergence of T_c with respect to the number of configurations and supercell size. For this purpose, we generated the following six configuration ensembles.

First, we generated one configuration ensemble consisting of all possible cation configurations for the conventional unit cell of the Th_3P_4-type structure consisting of 28 atoms

($4Mg_2GeO_4$, 12 cation sites); the lattice vectors of this cell are $(a, 0, 0)$, $(0, a, 0)$, and $(0, 0, a)$. At the 12a sites, 8 Mg and 4 Ge atoms were placed. Therefore, the number of possible configurations is ${}_{12}C_8 = {}_{12}C_4 = 495$ of which only 15 are irreducible.

Next, we prepared a $\sqrt{2} \times \sqrt{2} \times 1$ supercell consisting of 56 atoms ($8Mg_2GeO_4$, 24 cation sites); lattice vectors are $(a, a, 0)$, $(-a, a, 0)$, and $(0, 0, a)$. For this supercell, we generated four ensembles. The first one consists of all possible configurations, i.e., ${}_{24}C_{16}$ =735,471 in total, of which only 23,253 are symmetrically distinct. In addition, we generated three ensembles of configurations by cation interchange. These ensembles are generated for testing convergence with respect to the number of configurations. They are incomplete ensembles and do not represent a fully disordered structure. The procedure is schematically depicted in Fig. 2. We started with the ordered structure containing the 24 cations (16 Mg and 8 Ge ions) in their respective Wyckoff sites of the $I\bar{4}2d$-type phase. This configuration is one of the three equivalent lowest-enthalpy configurations (Conf. 1 in Fig. S1 [36]) and corresponds to the leftmost configuration in Fig. 2.) We refer to it as the "zero-interchange structure". Then we sequentially interchanged Mg/Ge pairs once. These single interchanges produce 128 (16×8) configurations where only 4 are irreducible, each with its distinct multiplicity. We refer to this first generation of structure as "one-interchange" configurations. Starting from these 128 configurations, we repeated this process and produced 3360 configurations among which 120 are irreducible "two-interchange" configurations. In the same way, we generated 31360 "three-interchange" configurations, among which 980 are irreducible. Therefore, we generated three ensembles of one-, two-, three-interchange configurations consisting of 5 (1+4), 125 (1+4+120), and 1105 (1+4+120+980) irreducible configurations, respectively.

Finally we prepared a supercell consisting of 224 atoms ($32Mg_2GeO_4$, 96 cation sites) with lattice vectors $(2a, 0, 0)$, $(0, 2a, 0)$, and $(0, 0, 2a)$. For this supercell, we did not generate an ensemble of all possible configurations, since its number is ${}_{96}C_{64} \sim 2.97 \times 10^{25}$ and too challenging. Instead, we generated one ensemble of 2048 one-interchange configurations among which 16 are symmetrically distinct.

C. Computational details

Calculations were performed using the local-density approximation [27] to density-functional theory. For all atomic species, Vanderbilt-type pseudopotentials [28] were gen-

erated. The valence electron configurations and cutoff radii for the pseudopotentials were $2s^2 2p^6 3s^2$ and 1.6 a.u. for Mg, $4s^2 4p^1 3d^{10}$ and 1.6 a.u. for Ge, and $2s^2 2p^4$ and 1.4 a.u. for O, respectively. Cutoff energies for the plane-wave expansion are 70 Ry. The $2 \times 2 \times 2$ **k**-point mesh was used for the 56-atom supercell. For structural optimization under arbitrary pressures between 100 and 800 GPa, we used the variable-cell-shape damped molecular dynamics algorithm [29, 30]. Dynamical matrices were calculated on the $2 \times 2 \times 2$ **q** mesh using density-functional perturbation theory [31, 32]. The vibrational contribution to the partition function was taken into account within the quasi-harmonic approximation (QHA) [26, 33, 35]. The $8 \times 8 \times 8$ **q**-point mesh was used for the QHA summation. All calculations were performed using the Quantum-ESPRESSO [34] and the `qha` software [35].

IV. RESULTS AND DISCUSSION

A. Convergence test results

To test the convergence of T_c with respect to the supercell size and the number of configurations, we calculated constant-volume heat capacity C_V for the six ensembles of configurations described above in fixed cubic cells with a lattice constant of 10.3 a.u., roughly corresponding to ∼200 GPa (Fig. 3); $E_i(V)$ in eq. 1 were obtained by relaxing only atomic positions, not the cell shape.

In the 28-atom conventional unit cell, C_V from all possible 15 irreducible configurations has a peak at ∼2100 K. Its full width at half maximum (FWHM) is considerably large and over ∼2000 K. In the $\sqrt{2} \times \sqrt{2} \times 1$ supercell consisting of 56 atoms, C_V from all possible 23,253 configurations has a peak at 2100 K (Fig. 3). Its FWHM is ≈ 1000 K, following the expected $1/\sqrt{N}$ scaling when compared to the FWMH of the 28-atom cell calculation. For one-, two-, three-interchange configurations, the peak in C_V narrows down with increasing the number of configurations (see Fig. 3). The peak temperature in $C_V(T)$ obtained using configuration ensembles generated by one-, two-, and three-interchanges are 2500, 2300, 2200 K, respectively, converging to that from all possible configurations, 2100 K. Finally, in the 224-atom supercell, C_V was calculated from the ensemble consisting of the 16 irreducible configurations by one-interchange. The peak in C_V in this case is at 2300 K (Fig. 3), being close to those from the configurations generated by one- and two-interchanges in the

$\sqrt{2} \times \sqrt{2} \times 1$ supercell.

This exercise indicates that a) when "all" possible configurations in ensembles of 28 and 56 atoms are used, the peak position in C_V (T_c) changes from ∼2000 K to ∼2100 K, while b) the FWHM follows the expected $1/\sqrt{N}$ scaling, with N being the number of atoms in the supercell; c) ensembles with fewer configurations that fail to represent the fully disordered structure also display a peak in C_V that converges with the increasing number of configurations to that obtained using "all" configurations. When going from "two-interchange" to "all" configurations in the 56-atom supercell, T_c decreases ∼200 K (∼9%); however, d) T_c obtained with the same number of cation interchanges decreases steadly by increasing the number of configurations, i.e., in going from 128 configurations (4 irreducible) in the 56-atom supercell to 2048 (16 irreducible) in the 224-atom one, T_c decreases by 200 K (∼8%). Therefore, we will refine the T_c calculation using the 125 configurations generated by up to two cation interchanges in the 56-atom supercell to estimate T_c in this ODT. We expect an uncertainty in T_c around ± 200–300 K.

To check the validity of our results in the two-interchange configuration ensemble, we calculated the probability of occurrence of the ith irreducible configuration given in Eq. 2. The probability calculated from the 125 two-interchange and all 23,253 configurations are shown in Fig. 4. For both configuration ensembles, the temperature dependence of the probabilities exhibits typical behavior expected in the ODT. Below T_c, the probability of the $I\bar{4}2d$-type phase is ∼1; the phase is cation ordered. As temperature increases, it abruptly decreases around T_c, while those of other configurations increase. At higher temperatures, all probabilities become comparable indicating a disordered phase. Since the behavior of probabilities in both ensembles are qualitatively the same, the two-interchange configuration ensemble can capture the ODT. Had we used a much larger supercell, the probability variation as well as the peak in C_V would be much sharper.

The difference of 200 K in T_c calculated from two-interchange and all configuration ensembles is also related to the degree of disorder, i.e., site occupancy ($q^{\mathrm{Mg}}_{\mathrm{Mg}}$ and $q^{\mathrm{Mg}}_{\mathrm{Ge}}$ in Eq. 3). Fig. 5 shows the temperature dependence of $q^{\mathrm{Mg}}_{\mathrm{Mg}}$ and $q^{\mathrm{Mg}}_{\mathrm{Ge}}$ for the configuration ensembles generated by one-, two-, and three-interchanges in the 56-atom supercell. At 0 K, the structure is $I\bar{4}2d$-type and fully ordered; $q^{\mathrm{Mg}}_{\mathrm{Mg}}$ and $q^{\mathrm{Mg}}_{\mathrm{Ge}}$ of the $I\bar{4}2d$-type phase are 1 and 0, respectively. As temperature increases and gets close to T_c, $q^{\mathrm{Mg}}_{\mathrm{Mg}}$ decreases and $q^{\mathrm{Mg}}_{\mathrm{Ge}}$ increases. In a fully disordered structure above T_c, Mg occupancy on all cation sites would be 2/3

(note that the number of Mg atoms is double that of Ge). As the number of interchanges increases, Mg occupancies approach the ideal value but differ from it, indicating that the structure is still partially disordered above T_c. Increasing the number of interchanges results in the all configuration ensemble. When all 23,253 configurations are used, Mg occupancy on all cation sites is always 2/3, even at 0 K, since all cation sites are equivalent when the supercell shape corresponds to that of the cubic phase, as done in these tests. Even if the supercell shape is relaxed, the ground state structure is threefold degenerate, corresponding to tetragonal configurations with the c-axis oriented along x, y, and z directions. In nature, one might see domains, polycrystalline samples resulting from local symmetry breaking, which does not occur in this type of calculation [36]. Nevertheless, this method clearly shows there is a single (though degenerate) predominant atomic configuration at low temperatures and identifies a peak in C_V that represents an ODT, as previously shown in the case of the ice-VIII to -VII transition [26].

B. ODT phase boundary

Results reported in this section were generated with the two-interchange ensemble of the 56-atom $\sqrt{2} \times \sqrt{2} \times 1$ supercell. Full structural relaxation was performed for each configuration and vibrational effects were included. C_P profiles at several pressures obtained using static free energy calculations (C_P^{st}) are shown in Fig. 6(a). The peak in C_P^{st} can be easily identified. Including the vibrational free energy contribution to the total free energy, a Debye-like contribution is added to C_P^{st} producing C_P^{st+vib}. The peak in C_P^{st+vib} appears as a hump in the Dulong-Petit regime of C_P^{st+vib} (Fig. 6(b)). The peak would have appeared very sharp if the calculation could have been carried out with an infinitely large supercell and number of configurations. By adding only the ZPM energy, E_{ZPM}, the heat capacity (C_P^{st+zpm}) still resembles C_P^{st}, except that T_c lowers by ∼100 K at 200 GPa (Fig. 6(c)). This temperature shift is essentially a volume effect caused by the expansion of the equilibrium volume upon inclusion of E_{ZPM}. Similarly, signs of the ODT can be found in bulk modulus and thermal expansivity as extremes at T_c in their differences between $I\bar{4}2d$-type and Th_3P_4-type ($I\bar{4}3d$) phase values (Fig. S2).

With increasing pressure, T_c, i.e., the peak temperature in C_P, increases producing the phase boundary shown in Fig. 6(d). This happens because the enthalpy difference between all

configurations and the ground state one, the ordered $I\bar{4}2d$-type phase, increases with pressure as shown in Fig. S3. Among the 125 configurations, the $I\bar{4}2d$-type phase has the lowest enthalpy at all pressures investigated here. The four irreducible configurations generated by one-interchange of cations are more similar to the ordered ground state structure and tend to have lower enthalpies than the 120 irreducible configurations produced by two-interchanges, with some exceptions. This behavior of T_c, i.e., the positive Clapeyron slope is opposite to that observed in the ice-VII to -VIII ODT. In the case of ice, all configuration enthalpies converge to a single value under pressure, that of ice X. This is because the ice ODT precedes and turns into a hydrogen-bond symmetrization transition under pressure [26]. Besides, in the present ODT T_c is only slightly altered by quantum effects, e.g, ZPM or thermal excitation effects. It takes place above the Debye temperature, θ_{Debye}, in the Dulong-Petit regime of C_V. Therefore, it has a classical origin and can be reasonably well addressed using the static partition function in Eq. 1. The positive Clapeyron slope also reflects a small volume increase of 0.1% across the ODT (see next Section). This result does not appear to be an artifact of the limited number of configurations, suggesting this ODT is a weakly first order transition. Only much larger supercell calculations might be able to resolve this issue.

C. ODT in the post-PPV transitions

The following dissociation and recombination post-PPv transitions were predicted in the MgO-GeO_2 system [24]:

Dissociation - $MgGeO_3$ (PPv) $\rightarrow$ Mg_2GeO_4 ($I\bar{4}2d$-type) + GeO_2 (pyrite-type) at $\sim$ 175 GPa followed by the transition of GeO_2 from pyrite- to cotunnite-type, which is not affected by the order-disorder transition;

Recombination - $MgGeO_3$ (PPv) + MgO (B1-type) $\rightarrow$ Mg_2GeO_4 ($I\bar{4}2d$-type) at $\sim$ 173 GPa.

These transitions remain valid at low temperatures, but above T_c one should replace the $I\bar{4}2d$-type phase by the Th_3P_4-type one. The newly computed phase boundaries for these transitions are shown in Fig. 7. Both reactions have negative Clapeyron slopes, a common

behavior in pressure induced structural transitions involving an increase in cation coordination [37]. The ODT widens the stability fields of the dissociation products of $MgGeO_3$ PPv (GeO_2 and Mg_2GeO_4) and of the recombination product (Mg_2GeO_4) because the configuration entropy lowers the Gibbs free energy of Mg_2GeO_4 in the disordered Th_3P_4-type phase. The configuration entropy also decreases in magnitude the negative Clapeyron slopes of dissociation and recombination transitions ($dT/dP = \Delta V/\Delta S$) at high temperatures. The volume of the Th_3P_4-type phase is slightly larger than that of the $I\bar{4}2d$-type phase as listed in Table S1. This result is consistent with the positive Clapeyron slope and $\Delta S > 0$ across the transition from the $I\bar{4}2d$-type to the Th_3P_4-type phase.

V. CONCLUSION

We have predicted an order-disorder transition (ODT) in the cation sublattices of the $I\bar{4}2d$-type Mg_2GeO_4, a post-PPv phase in the Mg-Ge-O system. This type of prediction is uncommon and is not accomplished simply using modern materials discovery techniques (e.g., Refs. [2–7]). In addition to structural prediction, the ODT prediction requires effective statistical sampling of atomic configurations [26]. Besides, T_c may not be calculated directly by comparing Gibbs free energy as in a regular first order transition. Instead, T_c is obtained by calculating the position of a peak in $C_P(T)$ throughout this second order transition (or first order one with a very small volume change). In this study, this was accomplished using *ab initio* quasiharmonic (QHA) calculations on a 56-atom supercell. Although vibrational effects play an essential role in high temperature polymorphic transitions, harmonic or anharmonic vibrational effects play a secondary role in the present ODT.

Very recently, the cation-disordered Th_3P_4-type Mg_2GeO_4 was independently observed at pressures beyond 162 GPa in a diamond-anvil-cell experiment [38]. In that experiment, the cation-ordered $I\bar{4}2d$-type Mg_2GeO_4 was not observed. Kinetic hindrance effects due to the adopted quenching procedure likely prevented the ordered phase's observation. As pointed out earlier, the ground state structure is threefold degenerate and the coexistence of the three states at low temperatures could make the observation of the ordered phase more challenging.

The predicted $I\bar{4}2d$-type to Th_3P_4-type phase change expands toward lower pressures and temperatures the stability fields of the post-PPv dissociation/recombination prod-

ucts containing Mg_2GeO_4. The MgO-GeO_2 system is a partly low-pressure analog of the Earth/planet-forming MgO-SiO_2 system. Both $I\bar{4}2d$-type Mg_2GeO_4 and Mg_2SiO_4 were predicted to occur as post-PPv dissociation/recombination transition products. Therefore, the present study suggests that a similar ODT should also occur in the Mg and Si cation sublattices of $I\bar{4}2d$-type Mg_2SiO_4 at the high temperatures typical of the deep interiors of super-Earths [11, 12].

Finally, it should be noted that the Th_3P_4-type structure is a high temperature form of several rare-earth sesquisulfides, $RR'S_3$ (R,R'=lanthanoid or actinoid), with vacancies at cation sites [39, 40]. For example, Gd_2S_3 is stabilized in the orthorhombic α phase at low temperature and transforms to the Th_3P_4-type γ phase with vacancies at high temperature. As pointed out earlier [41], the $RR'S_3$ family of structures form an analog system to high-pressure phases of $MgSiO_3$ and Al_2O_3 (bridgmanite, PPv, and U_2S_3-type). Hence, the prediction of the Th_3P_4-type phase in this study strengthens further the structural relationship between Earth/planet-forming phases at ultrahigh pressures and rare-earth sesquisulfides.

Acknowledgments

K.U. acknowledges support of a JSPS Kakenhi Grant # 17K05627. R.M.W. acknowledges support of a US Department of Energy Grant DE-SC0019759. All calculations were performed at Global Scientific Information and Computing Center and in the ELSI supercomputing system at the Tokyo Institute of Technology, the HOKUSAI system of RIKEN, and the Supercomputer Center at the Institute for Solid State Physics, the University of Tokyo.

---

[1] R. M. Wentzcovitch, and L. Stixrude (eds.), Theoretical and computational methods in mineral physics: Geophysical Applications, Reviews in Mineralogy and Geochemistry, **71** (2010).

[2] C. W. Glass, A. R. Oganov, and N. Hansen, USPEX – Evolutionary crystal structure prediction, Comp. Phys. Commun. **175**, 713-720 (2006).

[3] D. C. Lonie and E. Zurek, XTALOPT: An open-source evolutionary algorithm for crystal structure prediction, Comp. Phys. Commun. **175**, 713-720 (2011).

[4] C. J. Pickard and R. J. Needs, Ab initio random structure searching, J. Phys. Condens. Matter **23**, 053201 (2011).

[5] Y. Wang, J. Lv, L. Zhu, and Y. Ma, CALYPSO: A method for crystal structure prediction, Comp. Phys. Commun. **183**, 2063-2070 (2012).

[6] S. Q. Wu, M. Ji, C. Z. Wang, M. C. Nguyen, X. Zhao, K. Umemoto, R. M. Wentzcovith, and K. M. Ho, An adaptive genetic algorithm for crystal structure prediction,J. Phys.: Condens. Matter **26**, 035402 (2014).

[7] F. Curtis, X. Li, T. Rose, Á. Vázquez-Mayagoitia, S. Bhattachary, L. M. Ghiringhelli, and N. Marom, GAtor: A First-Principles Genetic Algorithm for Molecular Crystal Structure Predction, J. Chem. Theory Comput. **14**, 2246-2264 (2018).

[8] M. Murakami, K. Hirose, K. Kawamura, N. Sata, and Y. Ohishi, Post-perovskite phae transition in $MgSiO_3$. Science **304**, 855-858 (2004).

[9] A. R. Oganov and S. Ono, Theoretical and experimental evidence for a post-perovsite phase of $MgSiO_3$ in Earth's D" layer, Nature **430**, 445-448 (2004).

[10] T. Tsuchiya, J. Tsuchiya, K. Umemoto, and R. M. Wentzcovitch, Phase transition in $MgSiO_3$ perovskite in the earth's lower mantle, Earth Planet. Sci. Lett. **224**, 241-248 (2004).

[11] K. Hakim, A. Rivoldini, T. Van Hoolst, S. Cottenier, J. Jaeken, T. Chust, and G. Steinle-Neumann, A new ab initio equation of state of hcp-Fe and its implication on the interior tructure and mass-radius relations of rocky super-Earths, Icarus **313**, 61-78 (2018).

[12] A. P. van den Berg, D. A. Yuen, K. Umemoto, M. H. G. Jacobs, and R. M. Wentzcovich, Mass-dependent dynamics of terrestrial exoplanets using ab initio mineral properties, Icarus **317**, 412-426 (2019).

[13] R. F. Smith, J. H. Eggert, R. Jeanloz, T. S. Duffy, D. G. Braun, J. R. Patterson, R. E. Rudd, J. Biener, A. E. Lazicki, A. V. Hamza, J. Wang, T. Braun, L. X. Benedict, P. M. Celliers, and G. W. Collins, Ramp compression of diamond to five terapascals, Nature **511**, 330-333 (2014).

[14] L. Dubrovinsky, N. Dubrovinskaia, V. B. Prakapenka, and A. M. Abakumov, Implementation of micro-ball nanodiamond anvils for high-pressure studies above Mbar, Nat. Commun. **3**, 1163 (2012).

[15] N. Dubrovinskaia, L. Dubrovinsky, N. A. Solopova, A. Abakumov, S. Turner, M. Hanfland, E. Bykova, M. Bykov, C. Prescher, V. B. Prakapenka, S. Petitgirard, I. Chuvashova, B.

Gasharova, Y. L. Mathis, P. Ershov, I. Snigireva, and A. Snigiev, Terapascal static pressure generation with ultrahigh yield strength nanodiamond, Sci Adv. **2**, e1600341 (2016).

[16] A. Dewaele, P. Loubeyre, F. Occelli, O. Marie, and M. Mezouar, Toroidal diamond anvil cell for detailed measurements under extreme static pressres, Nat. Commun. **9**, 2913 (2018).

[17] T. Sakai, T. Yagi, T. Irifune, H. Kadobayashi, N. Hirao, T. Kunimoto, H. Ohfuji, S. Kawaguchi-Imada, Y. Ohishi, S. Tateno, and K. Hirose, High pressure generation using double-stage diamond anvil technique: problems an equations of state of rhenium, High Pressure Res. **38**, 107-119 (2018).

[18] K. Umemoto, R. M. Wentzcovitch, and P. B. Allen, Dissociation of $MgSiO_3$ in th Cores of Gas Giants and Terrestrial Exoplanets, Science **311**, 983-986 (2006).

[19] K. Umemoto and R. M. Wentzcovitch, Two-stage dissociation in $MgSiO_3$ post-peroskite, Earth Plenet. Sci. Lett. **311**, 225-229 (2011).

[20] H. Niu, A. R. Oganov, X. Q. Chen, and D. Li, Prediction of novel stable compound in the Mg-Si-O system under exoplanet pressures, Sci. Rep. **5**, 18347 (2015).

[21] K. Umemoto, R. M. Wentzcovitch, S. Wu, M. Ji, C. Z. Wang, and K. M. Ho, Phase tansitions in $MgSiO_3$ post-perovskite in super-Earth mantles, Earth Planet. Sci Lett. **478**, 40-45 (2017).

[22] R. Dutta, E. Greenberg, V. B. Prakapenka, and T. S. Duffy, Phase Transitions beynd post-perovskite in $NaMgF_3$ to 160 GPa, Proc. Nat. Acad. Sci. **116**, 1934-19329 (2019).

[23] K. Umemoto and R. M. Wentzcovitch, Two-stages Dissociation of $NaMgF_3$ Post-Pervskite: A Potential Low-Pressure Analog of $MgSiO_3$ at Multi-Mbar Pressures, JP Conf. Proc. **4**, 011002 (2015).

[24] K. Umemoto and R. M. Wentzvocitch, Ab initio exploration of post-PPv transitionsin low-pressure analogs of $MgSiO_3$, Phys. Rev. Mat. **3**, 123601 (2019).

[25] F. Marumo and Y. Syono, The Crystal Structure of Zn_2SiO_4-II, a High-Pressure Phase of Willemite, Acta Cryst. B**27**, 1868-1870 (1971).

[26] K. Umemoto, R. M. Wentzcovitch, S. de Gironcoli, and S. Baroni, Order–disorder phase boundary between ice VII and VIII obtained by first princiles, Chem. Phys. Lett. **499**, 236-240 (2010).

[27] J. P. Perdew and A. Zunger, Self-interaction correction to density-functional aproximations for many-electron systems, Phys. Rev. B, **23**, 5048 (1981).

[28] D. Vanderbilt, Soft self-consistent pseudopotentials in a generalized eigenvalueformalism,

Phys. Rev. B, **41**, R7892 (1990).

[29] R. M. Wentzcovitch, Invariant molecular-dynamics approach to structural phase trnsitions, Phys. Rev. B **44**, 2358 (1991).

[30] R. M. Wentzcovitch, J. L. Martins, and G. D. Price, Ab Initio Molecular Dynamicswith Variable Cell Shape: Application to $MgSiO_3$, Phys. Rev. Lett. **70**, 347 (1993).

[31] S. Baroni, S. de Gironcoli, A. Dal Corso, and P. Giannozzi, Phonons and related crystal properties from density-functional perturbation theoy, Rev. Mod. Phys. **73**, 515 (2001).

[32] P. Giannozzi, S. de Gironcoli, P. Pavone, and S. Baroni, Ab initio calculation o phonon dispersions in semiconductors, Phys. Rev. B **43**, 7231 (1991).

[33] D. Wallace, *Thermodynamics of Crystals*, John Wiley, Hoboken, N. J. (1972).

[34] P. Giannozzi, S. Baroni, N. Bonini, M. Calandra, R. Car, C. Cavazzoni, D. Ceresoli, G. L. Chiarotti, M. Cococcioni, I. Dabo, A. Dal Corso, S. de Gironcoli, S. Fabris, G. Fratesi, R. Gebauer, U. Gerstmann, C. Gougoussis, A. Kokalj, M. Lazzeri, L. Martin-Samos, N. Marzari, F. Mauri, R. Mazzarello, S. Paolini, A. Pasquarello, L. Paulatto, C. Sbraccia, S. Scandolo, G. Sclauzero, A. P. Seitsonen, A. Smogunov, P. Umari, and R. M. Wentzcovitch, Quantum ESPRESSO: a modular and open-source software projet for quantum simulations of materials, J. Phys.: Condens. Matter, **21**, 39502 (2009).

[35] T. Qin, Q. Zhang, and R. M. Wentzcovitch, and K. Umemoto, qha: A Python package for quasiharmonic free energy calculation for multi-configration systems, Comp. Phys. Commun. **237**, 199-207 (2019).

[36] See Supplemental Material at [URL will be inserted by publisher] for details of all configurations in $\sqrt{2} \times \sqrt{2} \times 1$ supercell.

[37] A. Navrotsky, Lower mantle phase transitions may generally have negative pressur-temperature slople, Geophys. Res. Lett. **7**, 709-711 (1980).

[38] R. Dutta, S. J. Tracy, J. Yang, P. C. Burnley, D. Smith, Y. Meng, S. Chariton, V. B. Prakapenka, and T. S. Duffy, Ultra-high pressure disordered eight-coordinated phase of Mg_2GeO_4: Analogue for super-Earth mantles, arXiv: 2101.00347 (2020).

[39] W. H. Zachariasen, Crystal Chemical Studies of the $5f$-Series of Elements. VI. he Ce_2S_3-Ce_3S_4 Type of Structure, Acta Cryst. **2**, 57-60 (1949).

[40] J. Flahaut, Sulfides, selenides, and tellurides. Handbook on the Physics and Cheistry of Rare-Earths, eds. Gschneidner K. A. Jr. and Eyring L. R. (North-Holland Amsterdam), **4**, 1 (1979).

[41] K. Umemoto, and R. M. Wentzcovitch, Prediction of an U_2S_3-type polymorph of Al_2O_3 at 3.7 Mbar, Proc. Nat. Acad. Sci. **105**, 6526-6530 (2008).

Figures

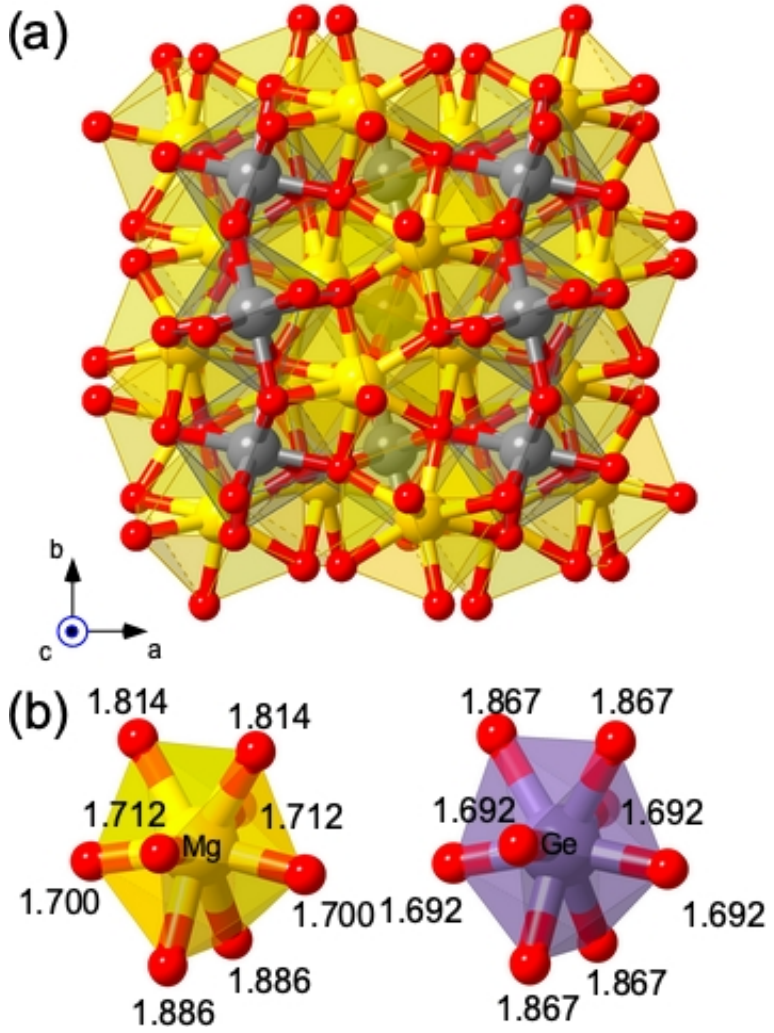

FIG. 1: (a) Crystal structure of $I\bar{4}2d$-type Mg_2GeO_4 containing 28 atoms per conventional unit cell. Yellow, grey, and red spheres denote Mg, Ge, and O ions, respectively. (b) Coodination polyhedra around Mg and Ge ions. Numbers next to the O atoms represent Mg-O and Ge-O bond-lengths in Angstroms at 400 GPa.

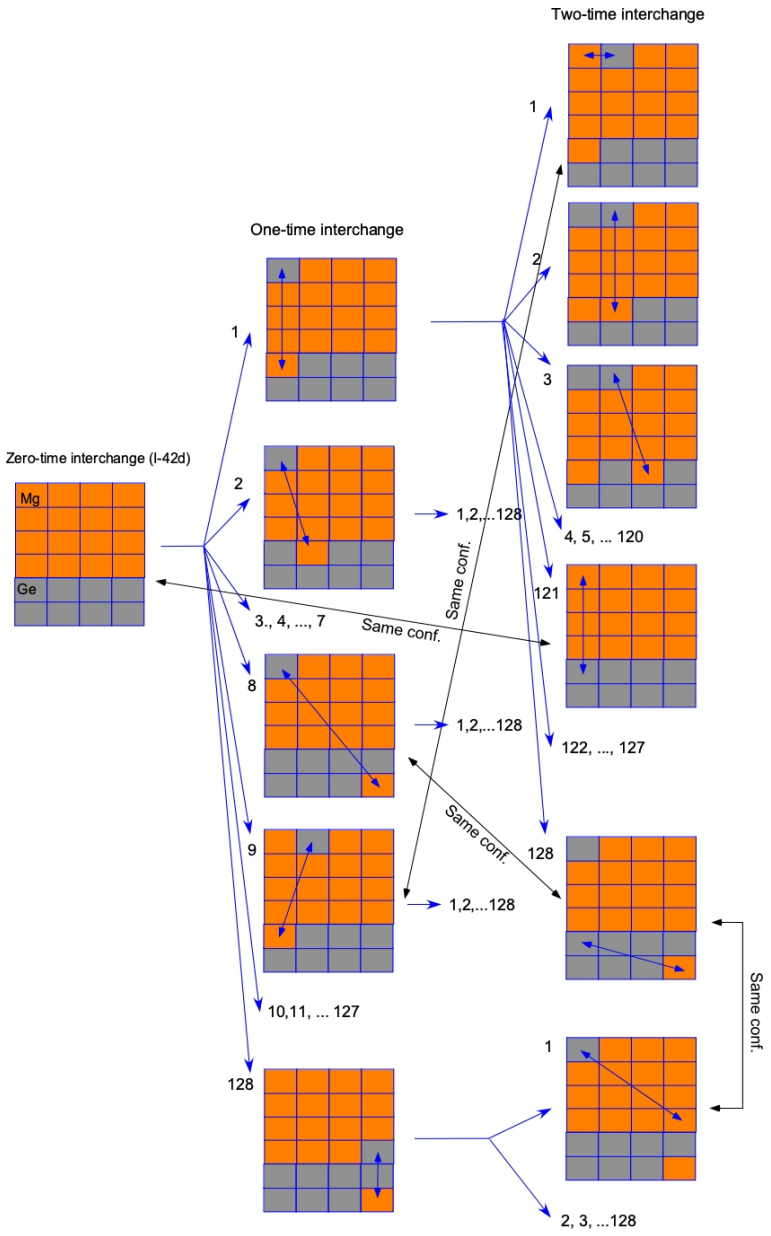

FIG. 2: Diagram showing the procedure to generate one- and two-interchange cation configurations starting from the $I\bar{4}2d$-type configuration (zero-interchange).

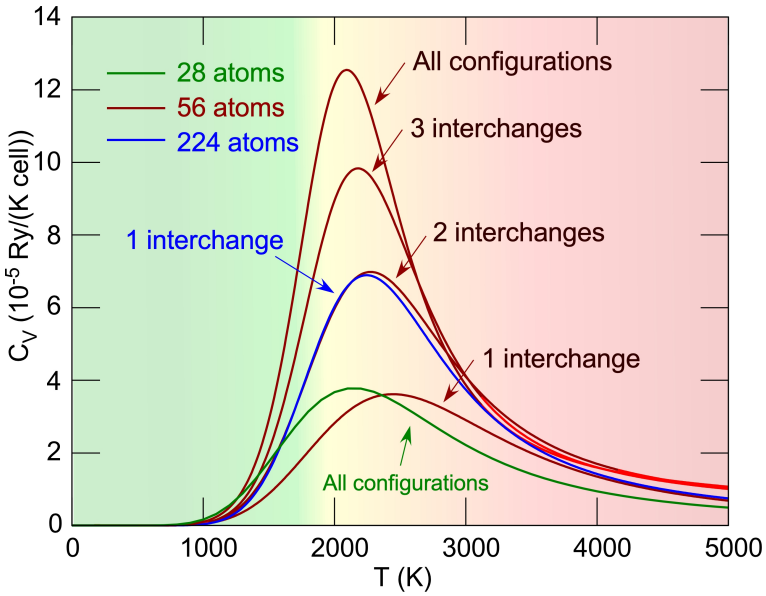

FIG. 3: Constant-volume heat capacity, C_V, calculated in several configuration ensembles generated using different supercell sizes: all configurations in the $1 \times 1 \times 1$ conventional unit cell (green line); all configurations and configurations generated by one-, two-, and three-interchanges of cations in the 56-atom supercell (red lines); configurations from one-interchange of cations in 228-atom supercell (blue line).

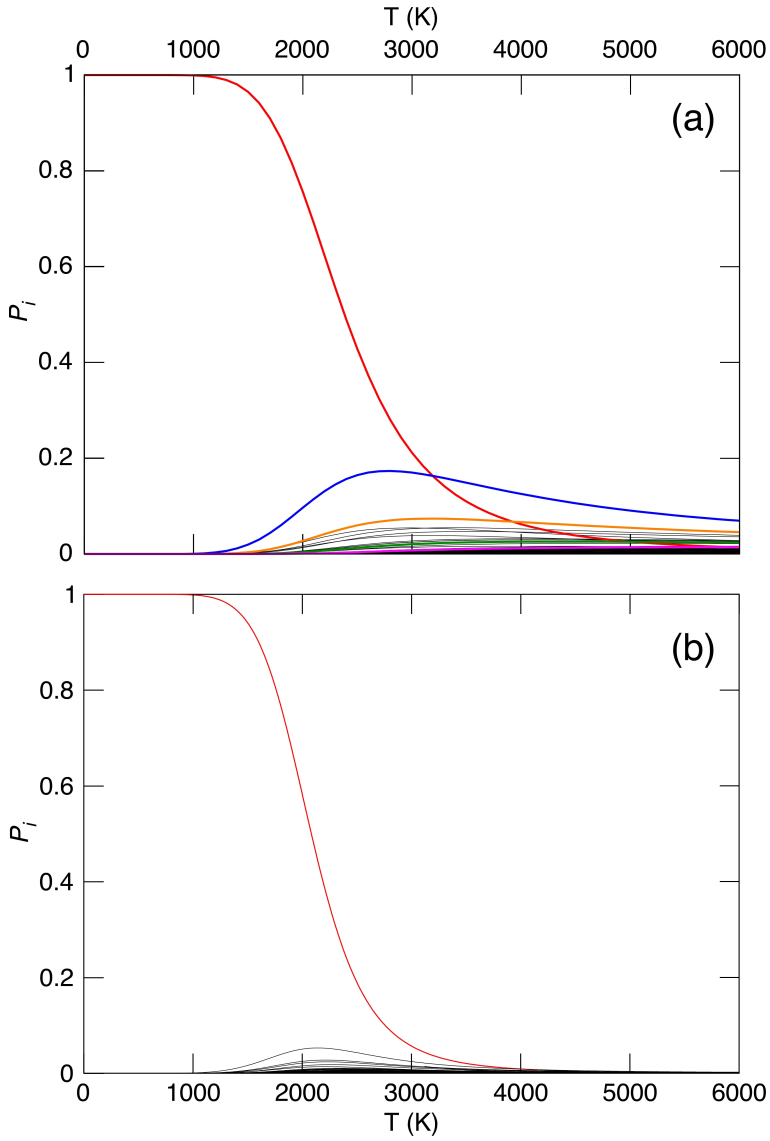

FIG. 4: Probabilities of the irreducible configurations (P_i in Eq. 2) in the ensembles from (a) two-interchange and (b) all configurations. In (a), the red line denotes the probability of the $I\bar{4}2d$-type phase. The other four colored and black lines represent the probabilities of 4 and 120 configurations generated by one- and two-interchanges from the $I\bar{4}2d$-type structure, respectively. In (b), the probability of the $I\bar{4}2d$-type phase is given by the summation of the two irreducible configurations with the same lowest energy [36]. Probabilities of the other 23,251 configurations are shown by the black lines.

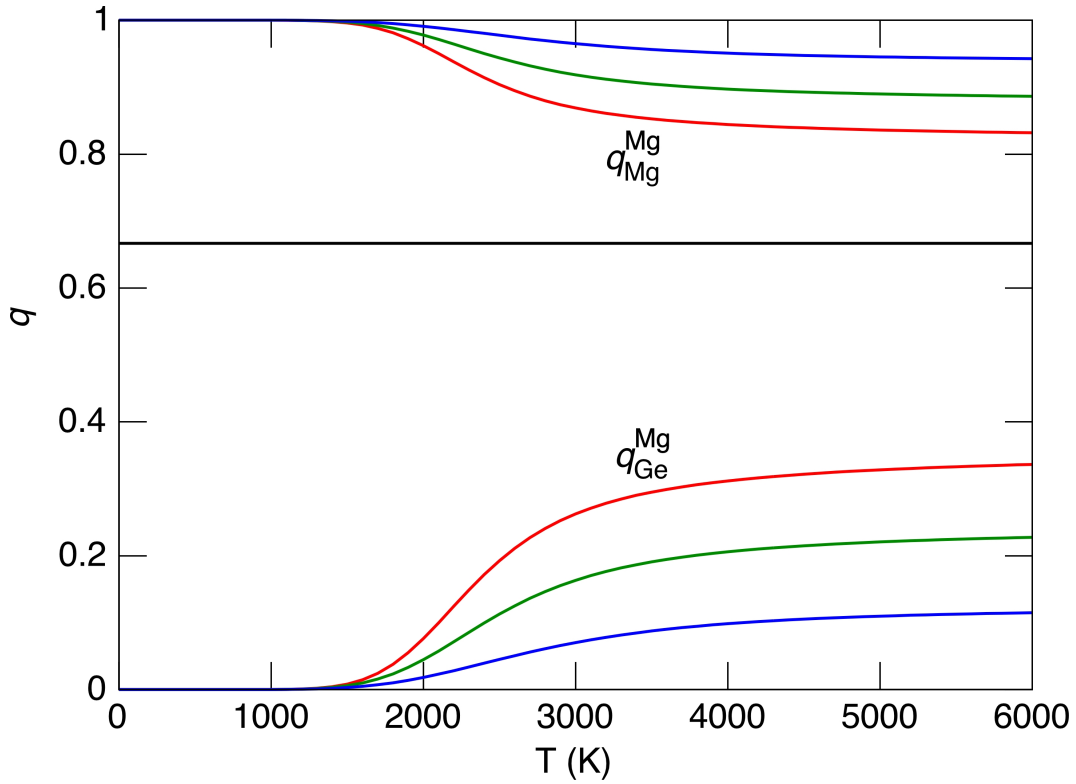

FIG. 5: Mg occupancies on Mg and Ge sites of $I\bar{4}2d$-type Mg_2GeO_4 in the 56-atom supercell: q^{Mg}_{Mg} and q^{Mg}_{Ge}. The blue, green, and red lines denotes q for the configuration ensembles generated by one-, two-, and three-interchanges. The sites are occupied by only Mg or Ge atoms when $q^{Mg}_{Mg} = 1$ or 0. For the fully ordered structure, i.e., $I\bar{4}2d$-type, $q^{Mg}_{Mg} = 1$ and $q^{Mg}_{Ge} = 0$. For the fully disordered structure, Th_3P_4-type, $q^{Mg}_{Mg} = q^{Mg}_{Ge} = 2/3$, denoted by the horizontal black line.

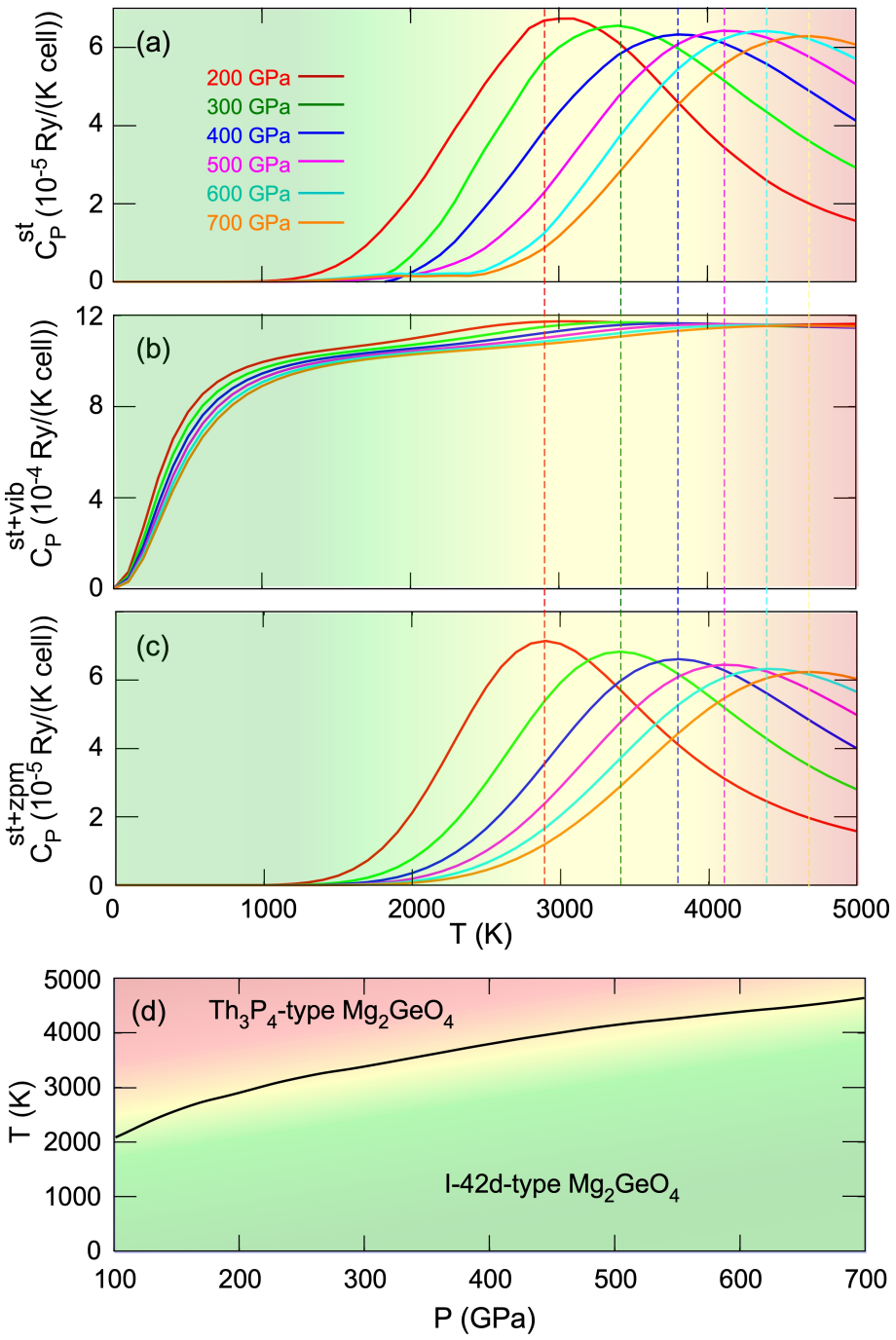

FIG. 6: Constant-pressure heat capacities, C_P, calculated using 125 configurations in the 56-atom supercell and (a) static free energies only (no vibrational effects included) (C_P^{st}), (b) free energies calculated using the QHA (C_P^{st+vib}), and (c) static free energy plus E_{ZPM} (C_P^{st+zpm}). Vertical dashed lines indicate the peak temperatures of C_P^{st+zpm}. (d) Phase boundary of the ODT between $I\bar{4}2d$-type and Th_3P_4-type Mg_2GeO_4 obtained from the peak temperatures in (c).

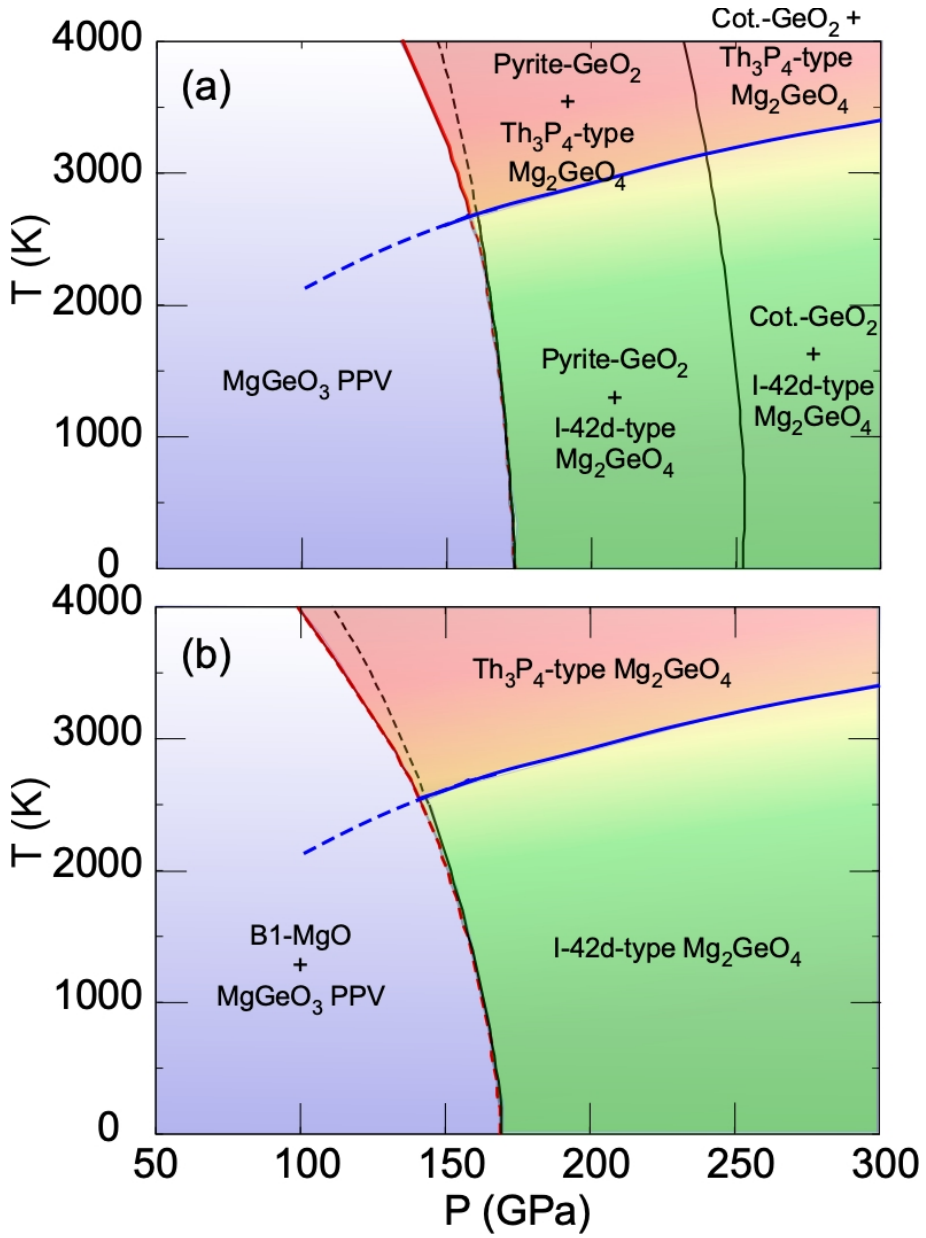

FIG. 7: Phase transition boundaries in the MgO-GeO_2 system. The blue solid lines show the ODT in Mg_2GeO_4 given by the peak temperature in C_P (Fig. 6(c)). The red lines denote the post-PPv phase boundaries involving Th_3P_4-type Mg_2GeO_4, while the black lines denote those involving $I\bar{4}2d$-type Mg_2GeO_4 calculated in Ref. [24]. The dashed lines represent the metastable continuation of these phase boundaries.